ACS APPLIED NANO MATERIALS

www.acsanm.org Article

Photoluminescence Properties of Ion-Implanted Er^{3+} Defects in 4H-SiCOI for Integrated Quantum Photonics

Joshua Bader, Shao Qi Lim, Faraz Ahmed Inam, Alexey Lyasota, Brett C. Johnson, Alberto Peruzzo, Jeffrey Colin McCallum, Qing Li, Sven Rogge, and Stefania Castelletto*

Cite This: https://doi.org/10.1021/acsanm.5c00085 Read Online

ACCESS | Metrics & More | Article Recommendations | Supporting Information

ABSTRACT: Atomic-size defects, known as color centers, hosted in solid-state materials, such as silicon carbide and diamond, are promising candidates for integration into chip-scale quantum systems. Specifically, the incorporation of these color centers within photonic integrated circuits may enable precise control over their inherent photophysical properties through strong light-matter interaction. Here, we investigate ion-implanted erbium (Er^{3+}) defects embedded in nanometric thin-film 4H-silicon-carbide-on-insulator (4H-SiCOI). Optimized implantation conditions and thermal annealing processes designed to enhance the photoluminescence excitation (PLE) emission characteristics of the Er^{3+} defect are reported. By examining key properties such as photoluminescence intensity, optical lifetime, and polarization, we present an analysis of ensemble Er^{3+} defects within 4H-SiCOI, providing insights into their potential for future quantum applications.

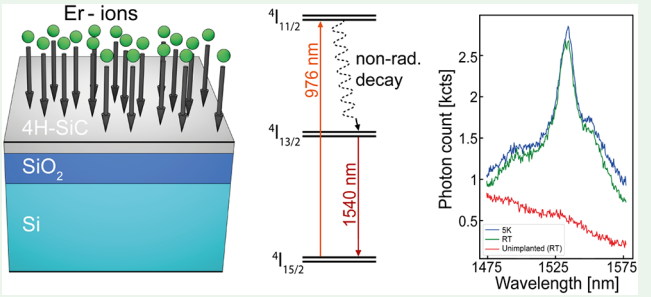

KEYWORDS: *photoluminescence, confocal microscopy, rare-earth dopants, ion implantation, silicon carbide on insulator*

INTRODUCTION

Silicon carbide (SiC) promises to evolve into a key platform for advancing quantum technologies. Over the past decade, efforts to establish SiC as a host for spin-photon-based quantum technologies have led to a notable advancement in its maturity.[1] Vacancy-related defects, such as the silicon vacancy,[2] divacancy,[3] or rare-earth dopants,[4,5] are optically active and incorporate optical spin read-out with reasonable spin coherence times; thus, they have attracted interest for quantum communication and computing applications as well as magnetometry.[6] These color centers can also act as single-photon emitters operating in the near-infrared and telecommunications band.[7] In addition to its unique advantages, SiC now offers industrial-scale wafer availability and compatibility with complementary metal-oxide-semiconductor (CMOS) processing strategies. These features position SiC to play a key role in advancing the realization of scalable quantum computers and nuclear spin-based quantum memory architectures.[8] Furthermore, its integration with fault-tolerant approaches[9] paves the way for large-scale quantum systems.

Among the various defects in SiC, the positively charged erbium ion (Er^{3+}) is of particular interest due to its $^4I_{13/2} \rightarrow {}^4I_{15/2}$ optical transition, which has been proven to be temperature-, semiconductor-, and material polytype-independent.[10] This particular transition occurs within the 4*f*-shell and is electrically shielded by its outer filled shells, which diminishes interaction with the surrounding material host.[11] In particular within the 4*f*-shell, Russell−Saunders coupling separates the excited state and ground state by ≈0.803 eV.[12] The associated electron spin is reported as $S = 1/2$.[13]

The previously identified infrared emission with a reported Er^{3+} emission line between 1528 and 1534 nm[10] into the depletion minima of silica fibers/optics[14] is of greatest interest for quantum and classical communication applications. Specifically, this Er^{3+} emission, hosted within 4H-SiCOI, may enable straightforward integration of Er^{3+}-based quantum emitters into low-loss existing fiber networks for long-distance quantum communication[15] via integrated quantum photonics.

Other novel incorporation of Er^{3+}defects include Er-doped yttrium orthosilicate Y_2SiO_5 and yttrium oxide Y_2O_3[16] for quantum memory applications.[17,18]

Compared to other materials, SiC and in particular silicon-carbide-on-insulator (SiCOI) provide a CMOS-compatible quantum-grade material platform, which accommodate $\chi^{(2)}$ (theoretically 30 pm/V)[19] and high $\chi^{(3)}$ susceptibilities, as well as a large Kerr nonlinearity ($\approx 10^{-18}$ m^2 W^{-1}).[20] Further accompanied by a dilute nuclear spin bath,[21,22] a high refractive index ($n = 2.6$), and a nonlinear refractive index ($n_2 = 8.6 \times 10^{-15}$ cm^2 W^{-1}).[19] Moreover, it provides an

Received: January 5, 2025
Revised: March 28, 2025
Accepted: April 1, 2025

https://doi.org/10.1021/acsanm.5c00085
ACS Appl. Nano Mater. XXXX, XXX, XXX−XXX

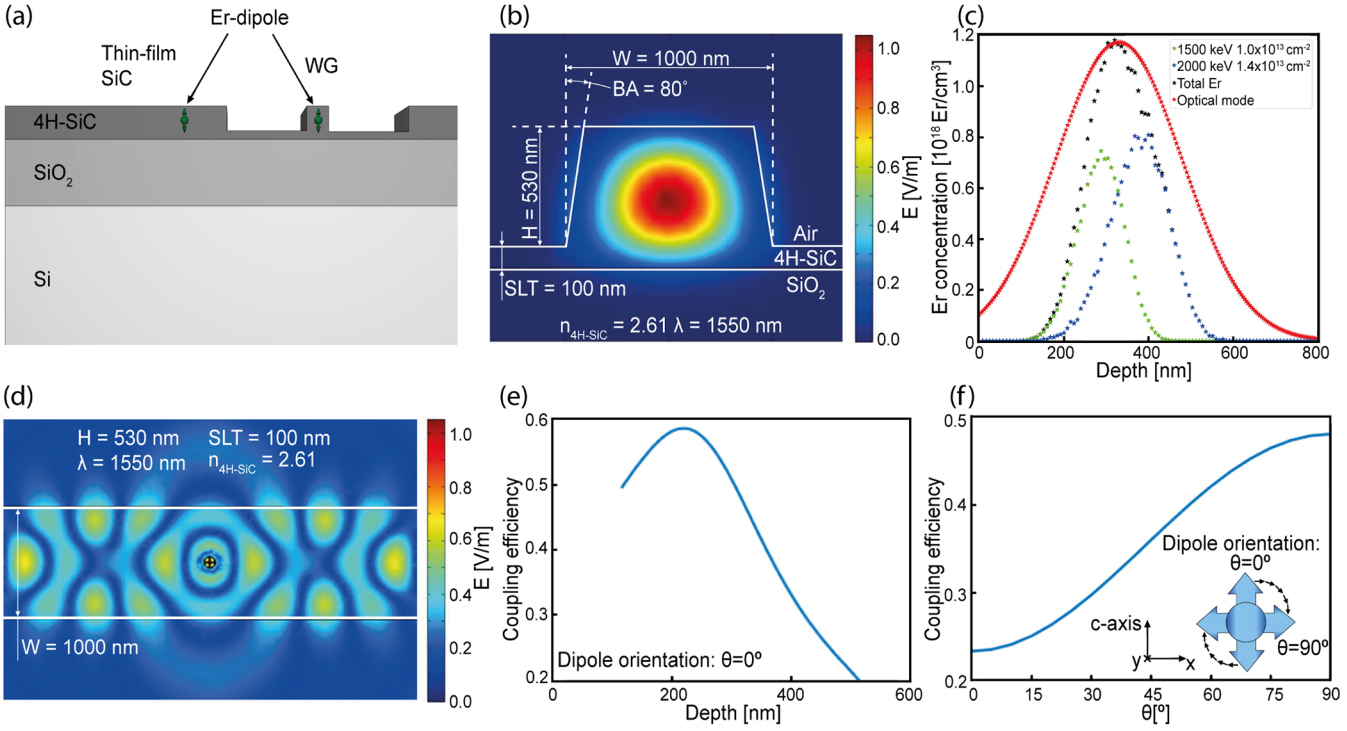

Figure 1. Waveguide mode, ion implantation profile, and Er^{3+} defect to waveguide coupling simulation: (a) schematic illustration of a photonic chip with two different sample architectures (SiC thin film and waveguide (WG)); (b) ANSYS Lumerical FDTD TE_{00} simulation of an air-cladded WG hosted in 4H-SiCOI with SLT: slap layer thickness, λ: light wavelength, BA: base angle of waveguide, H: waveguide height, $n^{4H\text{-}SiC}$: refractive index of 4H-SiC at desired wavelength, and W: waveguide width; (c) Er^{3+} implantation profile in 4H-SiCOI (black), obtained from Er^{3+} implantation at two different ion energies and fluences (green and blue), and the optical mode is shown in red; (d) simulated electric field from the vertical dipole emission coupled to a WG with a top view; (e) simulated coupling efficiency of a vertical dipole radiating into a WG structure versus depth of dipole location; (f) simulated impact of the dipole orientation within a SiCOI WG on the coupling efficiency for a dipole at 315 nm depth with schematic photon emission direction of the dipole indicated by arrows.

intrinsically wide bandgap of 3.26 eV that could lead to reduced quenching of the Er^{3+}photoluminescence at higher temperatures.[11]

Er^{3+}defects have been demonstrated previously in bulk 4H-SiC,[10,23] where it was shown via electron paramagnetic resonance (EPR) spectroscopy, that implanted Er^{3+}ions are most likely residing in Si sites, thus contributing to axial C_{3v} symmetry, although other hexagonal sites could also be occupied.[11] A comparison of implanted Er isotopes into hexagonal SiC polytypes indicated that approximately 10% of the implanted Er^{3+} ions are actively involved in the optically addressable defect.[24] So far, a demonstration of optically addressable Er^{3+} defects in thin-film 4H-SiCOI, which could take advantage of these unique intrinsic material capabilities, is still lacking. By utilizing the SiCOI platform, we aim to study the photoluminescence (PL), photoluminescence excitation (PLE), and polarization properties of the Er^{3+} defects in this material to determine that the optical properties are maintained and can be assessed in the thin film at a reduced Er concentration. This aims ultimately to achieve enhanced scalability for Er^{3+}-defect incorporation in SiCOI within photonic integrated circuits,[1] which increases the predictability of photonic device behavior and scalability when combined with various other semiconductor technologies.

Here, we report the first realization of ensemble Er^{3+} defects in thin-film 4H-SiCOI substantiated by insights into PL, PLE, and optical and polarization properties. Er ions were implanted directly into SiCOI with the goal of coupling the emission of these defects to a photonic integrated circuit (PIC). In particular, coupling the optically addressable Er^{3+} defects to a waveguide mode could enable control over the emission properties of the observed defect in a desired way. We find an operating temperature independence of the Er^{3+} emission line intensity with minor impact on the shape/line widths of the emission. Furthermore, an optical lifetime decrease is observed within the considered 4H-SiCOI samples with polarization properties indicating a C_{3V} symmetry of the Er^{3+} defect.

MATERIALS AND METHODS

Material Preparation. Our 4H-SiCOI samples consist of a 630-nm-thick 4H-SiC layer, bonded to a total of 2 μm silicon dioxide (SiO_2) on top of a 500 μm Si-layer handle, as shown schematically in Figure 1a. The 4H-SiCOI fabrication process is described in ref 25. In addition, we open 100-μm-wide trenches on the sample utilizing photolithography to avoid cracks during high-temperature annealing.

Er^{3+} Implantation. We simulated the Er-ion implantation concentration depth profiles with the stopping and range of ions in matter (SRIM) software package.[26] To achieve maximal overlap with the waveguide's propagating optical mode (as shown in Figure 1b), two Er implantations at different ion energies and fluences were performed: (1) 1.5 MeV 1.0×10^{13} Er/cm^2 and (2) 2 MeV 1.4×10^{13} Er/cm^2. The resulting Er concentration profile is a sum of these two profiles, as shown in Figure 1c, with its peak at 1.2×10^{18} Er/cm^3. The implantation was performed at 600 °C under vacuum to avoid amorphization of the SiC thin film.[11]

The simulated electric field as a result of a vertical Er^{3+} dipole emitter in the waveguide is shown in Figure 1d. The coupling efficiency between the Er^{3+} emitter and waveguide was also found to depend on both the depth location of the Er^{3+} relative to the surface

https://doi.org/10.1021/acsanm.5c00085
ACS Appl. Nano Mater. XXXX, XXX, XXX−XXX

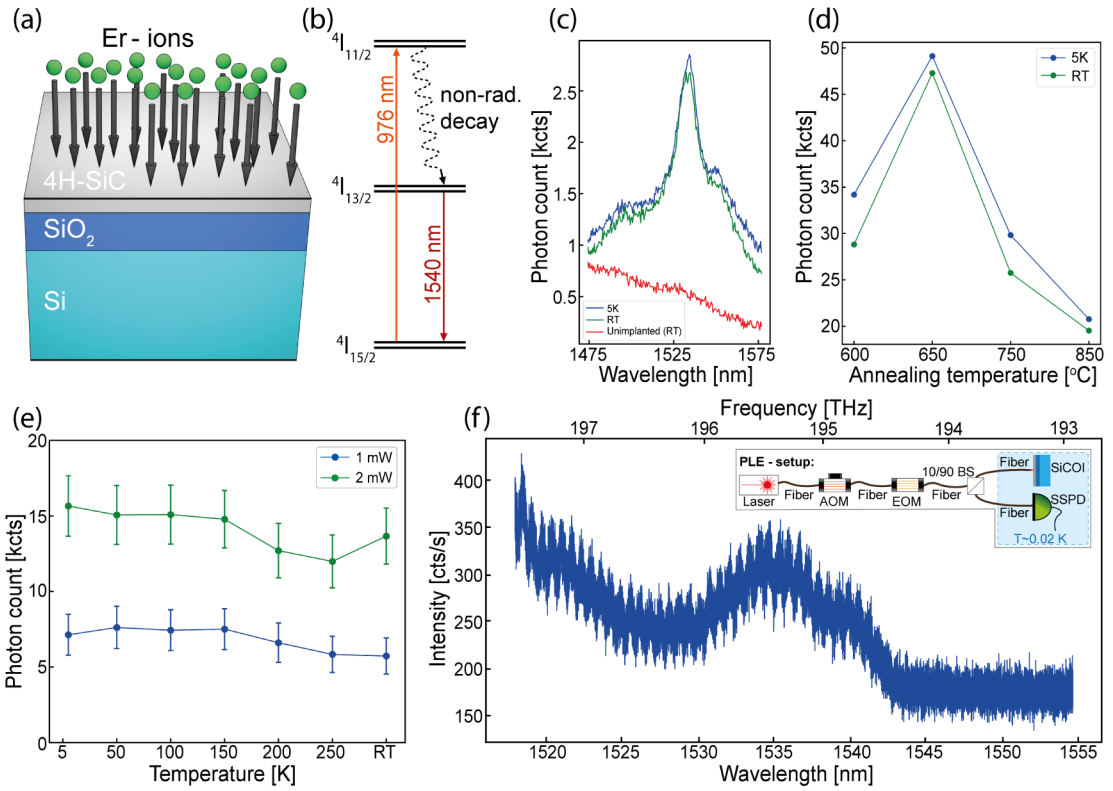

Figure 2. Ion implantation and photoluminescence measurements: (a) schematic illustration of the ion implantation process into 4H-SiCOI samples; (b) schematic energy-level diagram from the investigated transition; (c) PL spectrum of obtained Er^{3+} defects investigated measured at 5 K and RT with an additional measurement from unimplanted material at RT; (d) study of the Er^{3+} emission line intensity over annealing temperature, determined by integrating the obtained PL data points between 1528 and 1534 nm; (e) Er^{3+} emission line intensity traces observed over various measurement temperatures with data points determined by integrating the obtained PL measurement data between 1528 and 1534 nm; (f) PLE spectrum of 850 °C sample obtained at 0.02 mK with schematically illustrated experimental setup.

and angle of the Er^{3+} dipole ($\theta = 90°$ for a vertically oriented dipole along the 4H-SiC *c*-axis) as shown in Figure 1e and f), respectively.

Er^{3+} Purcell Enhancement Model in Thin Film and Waveguide. All electrodynamical calculations were carried out utilizing finite element method (FEM)-based Comsol Multiphysics radio frequency (RF) module. In these calculations, the color center/emitter is considered as a radiating point dipole, which is modeled as an oscillating point current source being driven at the emission frequency $\nu = c/\lambda$.[27,28] The scattering/PML boundary conditions are applied at the outer boundaries of the computational domain. The permittivity values utilized for SiC, SiO_2, and Si are based on the following reported values.[29,30]

The influence of the local environment can be fully expressed in terms of the classical local density of optical states (LDOS) model.[27] The dipole's spontaneous emission rates relative to a reference system are known to be exactly the same under both classical and quantum treatments.[27] In our calculations which are based on the classical electrodynamical treatment of the emitter as a radiating point dipole, the total power radiated by the dipole is calculated over a closed surface enclosing the point dipole emitter. The relative decay rate γ is then calculated as $\gamma = P/P_r$, where P_r is the power corresponding to the reference system. Here, the reference system is bulk SiC.

The coupling efficiency is calculated by scaling the time-averaged power flowing through the two ends of the SiC waveguide by the total power calculated over the surface enclosing the point dipole emitter.

Experimental Setup. Spectroscopy measurements were conducted with a custom-built confocal microscope equipped with either a 785 or 976 nm continuous-wave (cw) laser with a subsequent selection of a suitable dichroic mirror tailored to the applied excitation wavelength. We focused the excitation onto the samples with an Olympus 0.65NA 50× dry objective. The samples were placed inside a Montana cryostation operated with cycled helium to study the low-temperature properties of the Er^{3+} defect. In order to capture the emitted infrared photons, we employed a InGaAs avalanche photodiode (APD) as well as a Princeton Instruments LN_2-cooled spectrometer. (Schematic illustration of the experimental setup can be found in the Figure S1.)

We added a Thorlabs MC1F2 optical beam chopper to the excitation section of the confocal microscope, which modulated the 785 nm excitation for the optical lifetime measurement, as discussed below. Within the emission section, a 1550 ± 50 nm bandpass filter isolated the Er^{3+}-emission. Lastly, we implemented two full polarizers (FPs) and two $\lambda/2$ waveplates (HWPs) to investigate the polarization of the observed defect. The $\lambda/2$ waveplate within the emission section was replaced by a $\lambda/4$ waveplate (QWP) to provide further insights into the polarization.

The Er^{3+} emission obtained via photoluminescence excitation (PLE) spectroscopy is captured via an superconducting single-photon detector (SSPD).[31] The wavelength of the applied cw excitation is swept from 1517 to 1553 nm (197.6−193 THz) with 20 MHz increments. Furthermore, acousto-optic modulators (AOMs) and electro-optic modulators (EOMs) are employed to modulate the excitation with extinction ratios >160 dB. During the applied excitation, the detector current bias is configured to zero and resets to 20 μs after excitation, which reduces observed Joule heating from the detector introduced via the applied current and accelerates the SSPD recovery from the normal to superconducting state.[31] Following excitation, a digital counter records the number of emitted photons from the sample configured for an integration time of 160 μs. The excitation power, excitation pulse width, and excitation period were set to 17 μW, 20 μs, and 210 μs, respectively.

During the investigation, the sample was cooled to ≈0.02 K within a Leiden He_4/He_3 dry dilution refrigerator. That ensured low dark counts as well as minimized nonradiative rearrangements[32] of the

https://doi.org/10.1021/acsanm.5c00085
ACS Appl. Nano Mater. XXXX, XXX, XXX−XXX

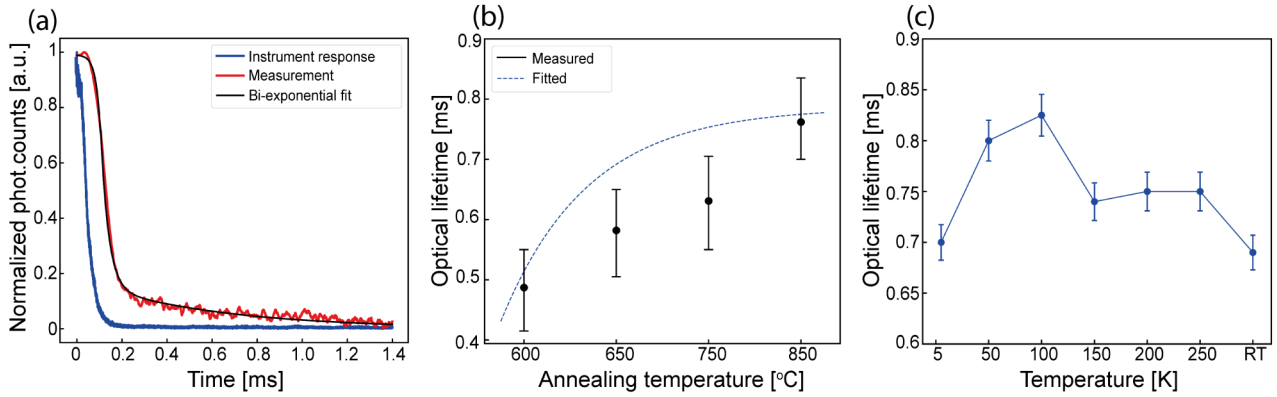

Figure 3. Optical lifetime properties of observed Er^{3+} defects: (a) observed time trace of an Er^{3+}defect; (b) impact of annealing temperature on optical lifetime with 785 nm excitation wavelength at RT; (c) impact of measurement temperature on optical lifetime with 785 nm excitation wavelength.

investigated Er^{3+} transition. A fiber, which is further connected to a 10:90 fiber-coupled beam splitter (BS), placed vertically above the sample applies the excitation and collects the emission which is then routed to a SSPD via the 10:90 BS.

RESULTS AND DISCUSSION

Photoluminescence. We investigated 4H-SiCOI samples with Er^{3+} defects introduced via ion implantation (Figure 2a). An energy-level diagram for the relevant Er^{3+} optical transition is shown in Figure 2b. Within this particular transition, the local crystal field causes a multilevel separation of ≈4 meV[33] from the $^4I_{15/2}$ ground state. That leads to internal dipole[12]-induced *f*-shell transitions. Certain implanted areas/sectors on the sample provided the Er^{3+} emission line as shown in Figure 2c. We conducted PL measurements at 5 K as well as at RT and found that the Er^{3+} emission line is present and stable at both of these temperatures, in agreement with previous reports.[10] We then performed an annealing study (shown in Figure 2d) which had an intrinsic lower boundary of 600 °C introduced by the performed implantation and an upper boundary of 1000 °C, where ablation damage was found on utilized samples. It can be seen that a 650 °C anneal provides the maximum Er^{3+} emission line signal. Here, all external parameters, such as the annealing atmosphere and duration, were kept constant (30 min in Argon (Ar)) based on initial findings from Choyke et al.[10]

According to the presented findings, this annealing temperature is sufficient to repair the implantation damage and minimize other effects inducing quenching of photoluminescence. However, the comparison between RT and 5 K revealed differences in the shape of the Er^{3+} emission line peak, which can be explained by utilizing the Debye−Waller Factor (DWF)[34] of ≈7.76 ± 0.27% at 5 K and ≈8.1 ± 0.28% at RT calculated as

$$\mathrm{DWF} = I_{\mathrm{Er\text{-}Em.}}/(I_{Er\text{-}Em.} + I_{\mathrm{SB}}) \quad (1)$$

where the intensity of the Er^{3+} emission line ($I_{\mathrm{Er-Em.}}$) was integrated from 1528 to 1534 nm and similarly for the sideband (I_{SB}) between 1450 and 1650 nm. The observed temperature independence of the Er^{3+} emission line intensity is further illustrated in Figure 2e for two different excitation powers.

We further investigated the PLE properties of the 850 °C sample at ≈0.02 K, as illustrated in Figure 2f, where Er clustering can be observed since we cannot identify single characteristic sites. The high detection sensitivity of the utilized SSPD detector led to the specific sample choice.

The observed behavior could be induced by residual damage, that is, vacancy-related defects, that do not recover during the annealing process. A small contribution could be related to intrinsic defects derived from the SiCOI processing, where defects could be present at $SiC-SiO_2$ interface or introduced during the thinning process.

Optical Lifetime. We characterized the optical lifetime of the Er^{3+} defect in our thin-film 4H-SiCOI samples by analyzing the PL transient resulting from the modulation of optical excitation. To our knowledge, optical lifetimes of Er^{3+} in thin-film 4H-SiCOI have not yet been characterized. In bulk 4H-SiC, patterned lifetimes of 1.16 ± 0.04 ms as well as unpatterned lifetimes of 1.56 ± 0.05 ms have been reported.[23] For this investigation, we modulated the excitation as elaborated previously and synchronized the detector output with the modulation trigger. Both the instrument response and Er^{3+} emission transients were recorded. A biexponential fit based on

$$\tau_{\mathrm{Fit}} = a\cdot e^{-\frac{b}{\tau_1}} + c\cdot e^{-\frac{d}{\tau_2}} \quad (2)$$

was performed on the Er^{3+} emission component of the transient. This gave optical lifetimes of $\tau_1 \approx 61 \pm 4$ μs and $\tau_2 \approx 582 \pm 30$ μs as illustrated in Figure 3a with an instrument response determined at ≈150 μs and a time resolution of 204.8 ns.

We performed optical lifetime measurements with all four annealed samples containing Er^{3+} defects, as illustrated in Figure 3b. We subsequently averaged the obtained τ_2 values from five different Er defects per sample and observed an overall lifetime variation of approximately 150 μs per annealing step with the shortest averaged lifetime provided by the 600 °C sample at 487 ± 63 μs. Furthermore, we identified an increase in the observed lifetime with higher annealing temperatures in agreement with previous reports[35] with average optical lifetimes determined at 582 ± 43 μs, 631 ± 34 μs, and 762 ± 56 μs for 650 °C, 750 °C, and 850 °C, respectively. Moreover, we fitted the data with an exponential fit based on

$$\tau_{\mathrm{Fit}} = \tau_{\mathrm{max}}\cdot\left(1 - e^{-\frac{T}{\tau_{\mathrm{meas}}}}\right) \quad (3)$$

to extrapolate the maximum achievable optical lifetime τ_{max}, which was determined to be 786 ± 62 μs, with T as a fitting parameter.

https://doi.org/10.1021/acsanm.5c00085
ACS Appl. Nano Mater. XXXX, XXX, XXX−XXX

We investigated the temperature dependence of the optical lifetime from 5 K to RT, as shown in Figure 3c, by conducting several measurements over a temperature range from 5 K to RT and observed an overall variation of 135 μs with the maximum lifetime observed at 100 K of 825 ± 42 μs. We identified that the sample annealed at the highest temperature produced the longest observed lifetime of 762 ± 89 μs within the 4H-SiCOI.

By simulating a dipole vertically oriented in a thin-film 4H-SiC at various depths, we compute Purcell's enhancement, $\gamma_{\text{thin film}}/\gamma_\infty$ from 0.8 to 1.1, as illustrated in Figure 4a, with a maximum around 50 nm just below the center of the material. The SiC layer enclosing the dipole emitter has a higher refractive index compared to the SiO_2 layer at the bottom and the surrounding air medium on the top. This refractive index asymmetry is subsequently leading to an electric field confinement with relatively high field amplitudes toward the higher indexed SiO_2 layer, thereby shifting the maximum of the decay rate curve from the center toward the higher indexed SiO_2 layer. Conversely within a waveguide structure, we do not expect a variation in the Purcell's enhancement for dipole location below the center of the structure, while Purcell's enhancement is suppressed for dipoles close to the waveguide surface, see Figure 4b. This can arise due to small electric field confinements at the WG/thin film interface, which could be caused by the considered structure.

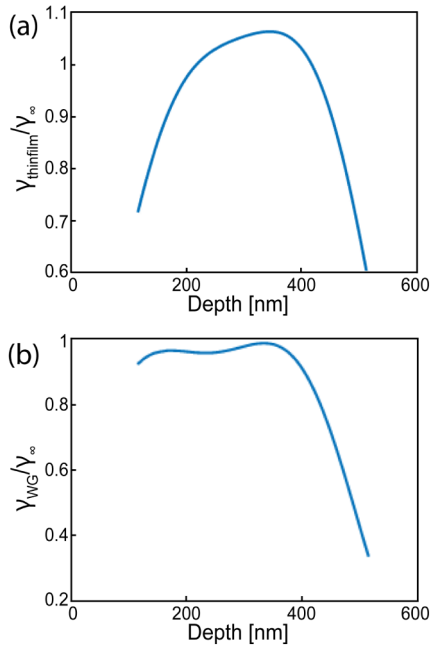

Figure 4. Dipole interaction simulation within thin-film 4H-SiC or WG hosted in 4H-SiCOI: (a) decay rate simulation of Er^{3+} dipoles within thin-film 4H-SiC relative to bulk (γ_∞); (b) decay rate simulation of Er^{3+} dipole within 4H-SiC waveguides relative to bulk (γ_∞).

Furthermore, geometry variations of the thin-film layer and WG can introduce significant modifications in the local density of states, as observed with Er^{3+}-doped silicon-on-insulator.[36] Here, other relevant observed lifetime reductions could be caused by the generally rearranged crystallinity of the thin-film 4H-SiC layer, which cannot be completely healed from implantation damage. This could have resulted in additional defects generated by implantation damage, providing non-radiative decay pathways. Therefore, the observed faster decay, described above, could be attributed to nonradiative effects, as the lifetime increases with annealing temperature with approximately 10% lifetime reduction caused by the thin-film layer as well as ensemble photon-emitter properties.

Absorption and Emission Polarization. We observed an absorption dipole by rotating a 780 nm HWP in combination with an FP in the excitation section of the experimental setup with a partial polarization ratio P_R of 0.38 (as shown in Figure 5a), calculated as[37]

$$I(\theta_{HWP}) = I_0 \cdot \cos^2(2 \cdot \theta_{HWP}) + I_{unpolarized} \quad (4)$$

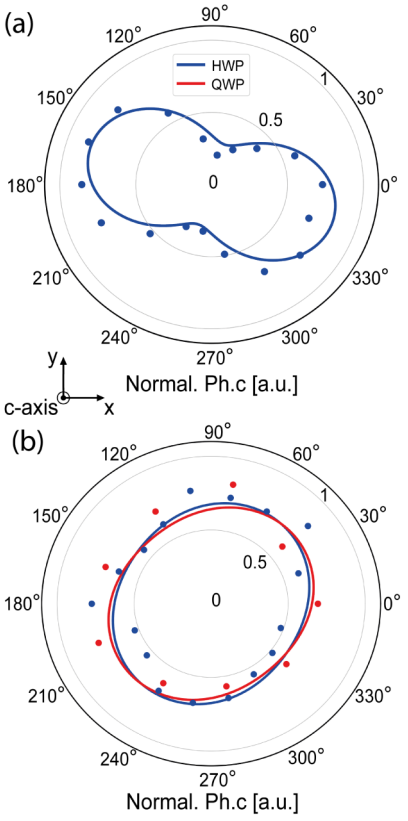

Figure 5. Polarization properties of observed Er^{3+} defects: (a) observed photon absorption dipole; (b) observed photon emission properties from the ensemble defect. Ph.C: Photon counts.

where I_0 and $I_{unpolarized}$ are the polarized and unpolarized light intensities, respectively. This subsequently led to the determination of the polarization ratio P_R, calculated as

$$P_R = I_0/(I_0 + I_{unpolarized}) \quad (5)$$

In terms of the emission polarization, we observed unpolarized dipole behavior (see Figure 5b) by rotating a 1550 nm HWP in combination with an FP in the emission section of the confocal microscope with the absorption 780 nm HWP set to its maximum. A QWP does not provide any further insights when it replaces the HWP within the emission section. A polarization ratio of ≈0.21 is determined with eqs 4 and 5. The fit for both measurements is calculated as

$$I = a + b \cdot \sin^2(\theta_{HWP} + \phi) \quad (6)$$

https://doi.org/10.1021/acsanm.5c00085
ACS Appl. Nano Mater. XXXX, XXX, XXX−XXX

with a, b, and ϕ as fit parameters.[38] The lack of emission polarization could be attributed to the presence of a nonradiative metastable state.[39] This indicates an orientation offset between the absorption and emission dipole, which could point to a $C3_V$ symmetry of the observed defects with a dominant alignment of the absorption dipole with the c-axis of the crystal.

In particular, the dipole offset could be caused by spin−orbit coupling, where the intrinsic electron spin interacts with orbital states[40] as well as nonradiative relaxation, which could be caused by vibrational modes within the SiC lattice.[41,42] Moreover, the excited $^4I_{13/2}$ state could also transit through different Stark levels before relaxing toward the $^4I_{15/2}$ ground state, which could contribute to different polarization characteristics, as observed here.[14] Furthermore, Er clustering and dipole−dipole interaction between Er defects could cause the observed behavior.

CONCLUSIONS AND OUTLOOK

Overall, we successfully demonstrated the characterization of ensemble Er^{3+} defects embedded in thin-film 4H-SiCOI. We provided insights into the photoluminescence, photoluminescence excitation, and optical and polarization properties for the specifically chosen Er concentration. With a strong observed independence of the operating temperature, this defect could be further investigated on a single-photon level at room temperature with the proposed annealing strategy applied, considering a direct implant into SiCOI. The observed optical lifetime is shorter in thin-film 4H-SiC layers compared to bulk material, which is supported by field confinement simulations. The C_{3V} symmetry from the observed defect seems it suitable for application in integrated quantum photonics, which can enhance certain favorable characteristics, as previously demonstrated in bulk SiC.[7,43] Furthermore, a recent work[44] studied theoretically the utilization of Er^{3+} defects embedded into ring resonators as integrated photon-pair sources generated by spontaneous four-wave mixing (SFWM) within 4H-SiCOI, where substantial advantages such as low two-photon absorption and free carrier absorption which negatively affect the performance, come into consideration.[45,46] This proposed design influences the spectral response to be compatible with quantum memories hosted in a Er^{3+}:Y_2SiO_5 matrix. The presented study points toward a new frontier where the composition of radiative defects within the telecommunication band and integrated quantum photonics applications play a crucial role.[47] Especially, 4H-SiCOI has potentially a bright future with its intrinsic material capabilities, like $\chi^{(2)}$ and $\chi^{(3)}$ processes with a dilute nuclear spin bath in a quantum- grade, CMOS-compatible matrix.

ASSOCIATED CONTENT

Data Availability Statement

The presented data are available upon request from the corresponding author.

Supporting Information

The Supporting Information is available free of charge at https://pubs.acs.org/doi/10.1021/acsanm.5c00085.

Additional experimental details including experimental setup description (PDF)

AUTHOR INFORMATION

Corresponding Author

Stefania Castelletto − *School of Engineering, RMIT University, Melbourne, VIC 3000, Australia;* orcid.org/0000-0002-8675-2291; Email: stefania.castelletto@rmit.edu.au

Authors

Joshua Bader − *School of Engineering and Centre for Quantum Computation and Communication Technology, School of Engineering, RMIT University, Melbourne, VIC 3000, Australia*

Shao Qi Lim − *Centre for Quantum Computation and Communication Technology, School of Physics, The University of Melbourne, Melbourne, VIC 3010, Australia*

Faraz Ahmed Inam − *Department of Physics, Aligarh Muslim University, Aligarh 202002, India;* orcid.org/0000-0003-3513-137X

Alexey Lyasota − *Centre of Excellence for Quantum Computation and Communication Technology, School of Physics, University of New South Wales, Sydney, NSW 2052, Australia;* orcid.org/0000-0001-6141-2349

Brett C. Johnson − *School of Science, RMIT University, Melbourne, VIC 3001, Australia;* orcid.org/0000-0002-2174-4178

Alberto Peruzzo − *Quandela, Paris 91300, France*

Jeffrey Colin McCallum − *Centre for Quantum Computation and Communication Technology, School of Physics, The University of Melbourne, Melbourne, VIC 3010, Australia;* orcid.org/0000-0002-6692-7728

Qing Li − *Electrical and Computer Engineering, Carnegie Mellon University, Pittsburgh, Pennsylvania 15213, United States;* orcid.org/0000-0002-8023-811X

Sven Rogge − *Centre of Excellence for Quantum Computation and Communication Technology, School of Physics, University of New South Wales, Sydney, NSW 2052, Australia*

Complete contact information is available at: https://pubs.acs.org/10.1021/acsanm.5c00085

Author Contributions

S.C., J.B., J.C.M., S.Q.L.: Conceptualization, experimental design, and methodology. Q.L., S.Q.L., J.C.M.: Fabrication and ion implantation. J.B., S.C., F.A.I., B.C.J., A.L., S.R.: Data acquisition, modeling, curation, visualization, and investigation. S.C., B.C.J., A.P. (partial): Supervision. J.B., S.C.: Writing original manuscript draft, reviewing, and editing. All authors contributed to writing and commenting on the final manuscript.

Notes

The authors declare no competing financial interest.

ACKNOWLEDGMENTS

J.C.M. acknowledges the Australian Government Australian Research Council under the Centre of Excellence scheme (No: CE170100012). Q.L. is supported by the National Science Foundation of the USA under Grant No. 2240420. F.A.I. acknowledges the financial support from the Department of Science and Technology (DST), India, for funding under the Core Research Grant (No. CRG/2021/001167). A.L. and S.R. are supported by the ARC Centre of Excellence for Quantum Computation and Communication Technology (Grant No.

CE170100012) and the Discovery Project (Grant No. DP210101784). The optical confocal characterization has been conducted in part within the RMIT Laboratories, partially funded by the ARC Centre of Excellence for Nanoscale BioPhotonics (No. CE140100003), and the LIEF scheme grant (No. LE140100131). We acknowledge the use of the NCRIS Heavy Ion Accelerator platform (HIA) for access and support to the ion implantation equipment at the Australian National University. This work was performed in part at the RMIT Micro Nano Research Facility (MNRF) in the Victorian Node of the Australian National Fabrication Facility (ANFF). The SSPD fabrication is performed at the NSW Node and ACT Node of the NCRIS-enabled ANFF. All authors acknowledge the work from Ruixuan Wang and Jingwei Li, who contributed to the fabrication of the investigated samples.

REFERENCES

(1) Lukin, D. M.; Dory, C.; Guidry, M. A.; Yang, K. Y.; Mishra, S. D.; Trivedi, R.; Radulaski, M.; Sun, S.; Vercruysse, D.; Ahn, G. H.; et al. others 4H-silicon-carbide-on-insulator for integrated quantum and nonlinear photonics. *Nat. Phot.* **2020**, *14*, 330−334.

(2) Liu, D.; Kaiser, F.; Bushmakin, V.; Hesselmeier, E.; Steidl, T.; Ohshima, T.; Son, N. T.; Ul-Hassan, J.; Soykal, Ö. O.; Wrachtrup, J. The silicon vacancy centers in SiC: Determination of intrinsic spin dynamics for integrated quantum photonics. *Npj Quantum Inf.* **2024**, *10*, 72.

(3) Sun, T.; Xu, Z.; Wu, J.; Fan, Y.; Ren, F.; Song, Y.; Yang, L.; Tan, P. Divacancy and silicon vacancy color centers in 4H-SiC fabricated by hydrogen and dual ions implantation and annealing. *Ceram. Int.* **2023**, *49*, 7452−7465.

(4) Astner, T.; Koller, P.; Gilardoni, C. M.; Hendriks, J.; Son, N. T.; Ivanov, I. G.; Hassan, J. U.; van der Wal, C. H.; Trupke, M. Vanadium in silicon carbide: Telecom-ready spin centres with long relaxation lifetimes and hyperfine-resolved optical transitions. *Quantum Sci. Technol.* **2024**, *9* (3), 035038.

(5) Bosma, T.; Lof, G. J. J.; Gilardoni, C. M.; Zwier, O. V.; Hendriks, F.; Magnusson, B.; Ellison, A.; Gällström, A.; Ivanov, I. G.; Son, N. T. others Identification and tunable optical coherent control of transition-metal spins in silicon carbide. *Npj Quantum Inf.* **2018**, *4*, 48.

(6) Niethammer, M.; Widmann, M.; Lee, S.-Y.; Stenberg, P.; Kordina, O.; Ohshima, T.; Son, N. T.; Janzén, E.; Wrachtrup, J. Vector magnetometry using silicon vacancies in 4 H-SiC under ambient conditions. *Phys. Rev. Appl.* **2016**, *6*, 034001.

(7) Radulaski, M.; Widmann, M.; Niethammer, M.; Zhang, J. L.; Lee, S.-Y.; Rendler, T.; Lagoudakis, K. G.; Son, N. T.; Janzen, E.; Ohshima, T.; et al. others Scalable quantum photonics with single color centers in silicon carbide. *Nano Lett.* **2017**, *17*, 1782−1786.

(8) Parthasarathy, S. K.; Kallinger, B.; Kaiser, F.; Berwian, P.; Dasari, D. B.; Friedrich, J.; Nagy, R. Scalable quantum memory nodes using nuclear spins in silicon carbide. *Phys. Rev. Appl.* **2023**, *19*, 034026.

(9) Bourassa, A.; Anderson, C. P.; Miao, K. C.; Onizhuk, M.; Ma, H.; Crook, A. L.; Abe, H.; Ul-Hassan, J.; Ohshima, T.; Son, N. T. others Entanglement and control of single nuclear spins in isotopically engineered silicon carbide. *Nat. Mater.* **2020**, *19*, 1319−1325.

(10) Choyke, W.; Devaty, R.; Clemen, L.; Yoganathan, M.; Pensl, G.; Hässler, C. Intense erbium-1.54-μm photoluminescence from 2 to 525 K in ion-implanted 4H, 6H, 15R, and 3C SiC. *Appl. Phys. Lett.* **1994**, *65*, 1668−1670.

(11) Babunts, R. A.; Vetrov, V. A.; Ilin, I. V.; Mokhov, E. N.; Romanov, N. G.; Khramtsov, V. A.; Baranov, P. G. Properties of erbium luminescence in bulk crystals of silicon carbide. *Phys. Solid State* **2000**, *42*, 829−835.

(12) Prezzi, D.; Eberlein, T.; Filhol, J.-S.; Jones, R.; Shaw, M.; Briddon, P.; Öberg, S. Optical and electrical properties of vanadium and erbium in 4 H-SiC. *Phys. Rev. B* **2004**, *69*, 193202.

(13) Baranov, P.; Ilyin, I. V.; Mokhov, E. Electron paramagnetic resonance of erbium in bulk silicon carbide crystals. *MSF* **1997**, *258*, 1539−1544.

(14) Digonnet, M. J. *Rare-earth-doped fiber lasers and amplifiers, revised and expanded*, 2nd ed; CRC press, 2001.

(15) Stevenson, P.; Phenicie, C. M.; Gray, I.; Horvath, S. P.; Welinski, S.; Ferrenti, A. M.; Ferrier, A.; Goldner, P.; Das, S.; Ramesh, R.; et al. others Erbium-implanted materials for quantum communication applications. *Phys. Rev. B* **2022**, *105*, 224106.

(16) Gupta, S.; Wu, X.; Zhang, H.; Yang, J.; Zhong, T. Robust millisecond coherence times of erbium electron spins. *Phys. Rev. Appl.* **2023**, *19*, 044029.

(17) Wang, S.-J.; Chen, Y.-H.; Longdell, J. J.; Zhang, X. Hyperfine states of erbium doped yttrium orthosilicate for long-coherence-time quantum memories. *J. Lumin.* **2023**, *262*, 119935.

(18) Jiang, M.-H.; Xue, W.; He, Q.; An, Y.-Y.; Zheng, X.; Xu, W.-J.; Xie, Y.-B.; Lu, Y.; Zhu, S.; Ma, X.-S. Quantum storage of entangled photons at telecom wavelengths in a crystal. *Nat. Commun.* **2023**, *14* (1), 6995.

(19) Cardenas, J.; Yu, M.; Okawachi, Y.; Poitras, C. B.; Lau, R. K.; Dutt, A.; Gaeta, A. L.; Lipson, M. Optical nonlinearities in high-confinement silicon carbide waveguides. *Opt. Lett.* **2015**, *40*, 4138−4141.

(20) Wu, I.; Guo, G. Second-harmonic generation and linear electro-optical coefficients of SiC polytypes and nanotubes. *Phys. Rev. B - Cond. Matt. Mater. Phys.* **2008**, *78*, 035447.

(21) Kanai, S.; Heremans, F. J.; Seo, H.; Wolfowicz, G.; Anderson, C. P.; Sullivan, S. E.; Onizhuk, M.; Galli, G.; Awschalom, D. D.; Ohno, H. Generalized scaling of spin qubit coherence in over 12,000 host materials. *Proc. Natl. Acad. Sci. U. S. A.* **2022**, *119*, No. e2121808119.

(22) Seo, H.; Falk, A. L.; Klimov, P. V.; Miao, K. C.; Galli, G.; Awschalom, D. D. Quantum decoherence dynamics of divacancy spins in silicon carbide. *Nat. Commun.* **2016**, *7* (1), 12935.

(23) Parker, R. A.; Dontschuk, N.; Sato, S.-I.; Lew, C.-K.; Reineck, P.; Nadarajah, A.; Ohshima, T.; Gibson, B.; Castelletto, S.; McCallum, J. others Infrared erbium photoluminescence enhancement in silicon carbide nano-pillars. *J. Appl. Phys.* **2021**, *130*, 145101.

(24) Pasold, G.; Albrecht, F.; Grillenberger, J.; Grossner, U.; Hülsen, C.; Witthuhn, W.; Sielemann, R. Erbium-related band gap states in 4H- and 6H-silicon carbide. *J. Appl. Phys.* **2003**, *93*, 2289−2291.

(25) Cai, L.; Li, J.; Wang, R.; Li, Q. Octave-spanning microcomb generation in 4H-silicon-carbide-on-insulator photonics platform. *Photonics Res.* **2022**, *10*, 870−876.

(26) Ziegler, J. F.; Ziegler, M.; Biersack, J. SRIM - The stopping and range of ions in matter. *Nucl. Instrum. Methods Phys. Res. B* **2010**, *268*, 1818−1823.

(27) Xu, Y.; Vučković, J.; Lee, R.; Painter, O.; Scherer, A.; Yariv, A. Finite-difference time-domain calculation of spontaneous emission lifetime in a microcavity. *J. Opt. Soc. Am. B* **1999**, *16*, 465−474.

(28) Novotny, L.; Hecht, B. *Principles of nano-optics*; Cambridge university press, 2012.

(29) Shaffer, P. T. Refractive index, dispersion, and birefringence of silicon carbide polytypes. *Appl. Opt.* **1971**, *10*, 1034−1036.

(30) Green, M. A. Self-consistent optical parameters of intrinsic silicon at 300 K including temperature coefficients. *Sol. Energy Mater. Sol. Cells* **2008**, *92*, 1305−1310.

(31) Berkman, I. R.; Lyasota, A.; De Boo, G. G.; Bartholomew, J. G.; Johnson, B. C.; McCallum, J. C.; Xu, B.-B.; Xie, S.; Ahlefeldt, R. L.; et al. Observing Er $^{3+}$+ + Sites in Si With an In Situ Single-Photon Detector. *Phys. Rev. Appl* **2023**, *19*, 014037.

(32) Palm, J.; Gan, F.; Zheng, B.; Michel, J.; Kimerling, L. Electroluminescence of erbium-doped silicon. *Phys. Rev. B* **1996**, *54*, 17603.

(33) Choyke, W.J.; Devaty, R. P.; Yoganathan, M.; Pensl, G.; Edmond, J.A.Fine Structure and higher lying transitions of Er^{3+} in 4H and 6H SiC*Shallow-Level Centers In Semiconductors-Proceedings Of The 7th International Conference*World Scientific1996297−302

https://doi.org/10.1021/acsanm.5c00085
ACS Appl. Nano Mater. XXXX, XXX, XXX−XXX

(34) Debye, P. Interferenz von roentgenstrahlen und waermebewegung. *Ann. Phys* **1913**, *348*, 49−92.
(35) Sullivan, S. E.; Ahn, J.; Zhou, T.; Saha, P.; Holt, M. V.; Guha, S.; Heremans, F. J.; Singh, M. K. Quasi-deterministic localization of Er emitters in thin film TiO2 through submicron-scale crystalline phase control. *Appl. Phys. Lett.* **2023**, *123* (25), 254001.
(36) Gritsch, A.; Weiss, L.; Fruh, J.; Rinner, S.; Reiserer, A. Narrow optical transitions in erbium-implanted silicon waveguides. *Phys. Rev. X* **2022**, *12*, 041009.
(37) Hecht, E. *Optics*; Pearson Education India, 2012; pp. 346.
(38) Wang, J.-F.; Liu, Z.-H.; Yan, F.-F.; Li, Q.; Yang, X.-G.; Guo, L.; Zhou, X.; Huang, W.; Xu, J.-S.; Li, C.-F. others Experimental optical properties of single nitrogen vacancy centers in silicon carbide at room temperature. *ACS Photonics* **2020**, *7*, 1611−1616.
(39) Berhane, A. M.; Jeong, K.-Y.; Bradac, C.; Walsh, M.; Englund, D.; Toth, M.; Aharonovich, I. Photophysics of GaN single-photon emitters in the visible spectral range. *Phys. Rev. B* **2018**, *97*, 165202.
(40) Dong, W.; Doherty, M.; Economou, S. E. Spin polarization through intersystem crossing in the silicon vacancy of silicon carbide. *Phys. Rev. B* **2019**, *99*, 184102.
(41) Kenyon, A. Recent developments in rare-earth doped materials for optoelectronics. *Prog. Quantum Electr.* **2002**, *26*, 225−284.
(42) Miniscalco, W. J. Erbium-doped glasses for fiber amplifiers at 1500 nm. *J. Lightwave Technol.* **1991**, *9*, 234−250.
(43) Babin, C.; Stöhr, R.; Morioka, N.; Linkewitz, T.; Steidl, T.; Wörnle, R.; Liu, D.; Hesselmeier, E.; Vorobyov, V.; Denisenko.; et al. A.; others Fabrication and nanophotonic waveguide integration of silicon carbide colour centres with preserved spin-optical coherence. *Nat. Mater.* **2022**, *21*, 67−73.
(44) Ramirez, P.M.C. T.; Gomez, J. S. S. D.; Becerra, G. J. R.; Ramirez-Alarcon, R.; Robles, M. G.; Salas-Montiel, R. Integrated photon pairs source in silicon carbide based on micro-ring resonators for quantum storage at telecom wavelengths. *Sci. Rep.* **2024**, *14*, 17755.
(45) Xing, P.; Ma, D.; Kimerling, L. C.; Agarwal, A. M.; Tan, D. T. High efficiency four wave mixing and optical bistability in amorphous silicon carbide ring resonators. *APL Photonics* **2020**, *5*, 076110.
(46) Xing, P.; Ma, D.; Ooi, K. J.; Choi, J. W.; Agarwal, A. M.; Tan, D. CMOS-compatible PECVD silicon carbide platform for linear and nonlinear optics. *ACS Photonics* **2019**, *6*, 1162−1167.
(47) Bader, J.; Arianfard, H.; Peruzzo, A.; Castelletto, S. Analysis, recent challenges and capabilities of spin-photon interfaces in Silicon carbide-on-insulator. *Npj Nanophoton.* **2024**, *1* (1), 29.

https://doi.org/10.1021/acsanm.5c00085
ACS Appl. Nano Mater. XXXX, XXX, XXX−XXX